



Risk assessment of copper-containing contraceptives: the impact for women with implanted intrauterine devices during clinical MRI and CT examinations

Wiebke Neumann¹ · Tanja Uhrig¹ · Matthias Malzacher¹ · Verena Kossmann¹ · Lothar R. Schad¹ · Frank G. Zoellner¹

Received: 13 August 2018 / Revised: 28 September 2018 / Accepted: 25 October 2018 / Published online: 19 November 2018

© European Society of Radiology 2018

Abstract

Objectives To assess the risks for implant users with copper-containing intrauterine devices (IUDs) during MR and CT examinations.

Methods A tissue-mimicking phantom suitable for all experiments within this study was developed. Seven different types of copper IUDs were evaluated. Heating and dislocation of each IUD were investigated at two clinically relevant positions in 1.5 T and 3 T MR scanners. Artifacts in the field of view caused by each tested IUD were determined for clinical MR and CT imaging.

Results No significant heating of any tested IUD was detected during MR measurements. The temperature increase was less than 0.6 K for all IUDs. Neither angular deflection nor translation of any IUD was detected. Artifacts in MR images were limited to the very vicinity of the IUDs except for one IUD containing a steel-visualizing element. Streaking artifacts in CT were severe (up to 75.5%) in the slices including the IUD.

Conclusion No significant risk possibly harming the patient was determined during this phantom study, deeming MR examinations safe for women with an implanted copper IUD. Image quality was more impaired for CT than for MR imaging and needs careful consideration during diagnosis.

Key Points

- Risk assessment of copper-containing IUDs with regard to heating, dislocation, and artifacts during MR and CT imaging.
- Neither significant heating nor dislocation was determined in MR; image quality was more impaired for CT than for MR imaging and needs careful consideration during diagnosis.
- The tested IUDs pose no additional risks for implant users during MR and CT examinations.

Keywords Intrauterine devices, copper · Patient safety · Magnetic resonance imaging · Phantoms, imaging · Tomography, X-ray computed

Abbreviations

| | |
|-------|---|
| ASTM | American Society for Testing Materials |
| FoV | Field of view |
| IUD | Intrauterine device |
| RF | Radiofrequency |
| TRUFI | True fast imaging with steady-state free precession |
| TSE | Turbo spin echo |

Wiebke Neumann and Tanja Uhrig contributed equally to this work.

✉ Wiebke Neumann
Wiebke.Neumann@medma.uni-heidelberg.de

¹ Computer Assisted Clinical Medicine, Medical Faculty Mannheim, Heidelberg University, 68167 Mannheim, Germany

Introduction

Nowadays, 60% of women of childbearing age use at least one form of contraception [1]. One of these forms is a long-acting reversible intrauterine device (IUD) implanted in the woman's uterus [2]. Newly developed smaller and frameless devices can also be used by nulliparous women [3]. In Europe, 12.4% of women aged 15–49 used a long-acting reversible contraceptive IUD in 2009 [4].

IUDs are classified into hormone- and metal-based IUDs. Various models of non-hormonal metal-containing IUDs are made of copper. One design approach includes a copper thread wound around a plastic stem. Another design connects multiple copper tubes on a surgical thread. Recently, a third design was introduced, consisting of a

shape memory alloy with several copper pearls strung on a spherical frame.

At the same time, diagnostic imaging procedures such as MR and CT have become crucial tools in the clinics. The latest innovations point to an increasing clinical use of 3 T [5] and even higher field strengths of MR systems. Naturally, those magnetic fields exclude several patient cohorts, such as implant users, from safely entering an MR examination. Numerous studies have evaluated the MRI risks for patients with deep brain stimulation electrodes. The main safety concern in these patients is heating at the electrode tips during MRI [6, 7].

Despite these concerns, the effects of different models of implanted copper IUDs during clinical 3 T MR and CT examinations have not been systematically investigated. This is surprising, as more than one in ten women of childbearing age in Europe, approximately 12 million women, have an implanted IUD [4].

Non-ferromagnetic conducting metals, as they are part of an IUD, may induce heating, undergo motion and torque, or affect image quality in MRI [8–10]. Gradients can cause eddy currents potentially leading to tissue heating. Radiofrequency (RF) pulses can induce thermal effects depending on the material's electrical conductivity [11]. Here, metallic implants may act as antennas. The employed RF wavelength depends on the magnetic field strength of the scanner and shortens with increasing field strength. Depending on the implant length in combination with the RF wavelength, i.e., field strength, local RF power deposition may increase. Potentially, this induces local heating damaging surrounding tissue [12].

A further risk arises from forces and torques, which implants experience in the presence of the static field [13–15]. Here, the magnetic susceptibility is considered a good measure of the occurring forces and torques [11].

Thus, introducing a copper IUD into the stray field, the bore, or even the field of view (FoV) during an MR scan poses risks to the patient that need careful consideration. Staff, such as radiologists and nurses, as well as maintenance and cleaning personnel, working around medical MR equipment may also be affected.

Additionally to the safety concerns, implants may impair the image quality of MRI exams due to deformations of the static magnetic fields [11]. The level of field deformation and thus severity of the image artifacts are determined by several properties such as the geometry, volume, and orientation of the implant within the scanner [13–15].

Although CT exams are not particularly contraindicated by IUDs, this imaging modality is also adversely affected by these implants as the density of the metallic components highly attenuates the X-ray beam [16]. An insufficient number of photons reach the detector leading to severe streaking, beam hardening, and aliasing artifacts [17]. Furthermore, dose-reducing developments in CT imaging struggle with more pronounced image artifacts [18] that may further be amplified by IUDs.

However, to date, no studies have investigated the influences of IUDs in CT imaging. In MRI, previous studies have tested only a few models at 1.5 T scanners [19–21]. Models that were only recently commercially available have not yet been assessed. Furthermore, no studies evaluated these in 3 T scanners. Hence, it is currently recommended that patients consult a gynecologist to check for potential dislocation of the IUD after an MR examination [22]. However, an additional gynecological follow-up examination has, as every medical test, intrinsic risks and cannot reverse the damage caused by excessive heating.

If copper IUDs posed no additional risk to the implant user, it would no longer be necessary to precautionarily exclude female volunteers with implanted IUDs from clinical MR studies or recommend additional gynecological examinations, as it sometimes occurs in clinical practice today.

The aim of the study was thus to address MR safety concerns and to assess the feasibility of diagnostic MR and CT examinations for women using copper-containing contraceptives. A study with a tissue-mimicking phantom was conducted to investigate possible heating, dislocation, and artifacts of various IUD designs.

Materials and methods

For all measurements, we adhered to the American Society for Testing Materials (ASTM) F2119, F2182, and F2213 standards [23–25] and the European Norm for MR systems for medical diagnostics EN60601-2-33 [26].

Tested IUDs

Seven commercially available copper-containing IUDs were obtained (Fig. 1).

Three IUDs (Cu380, Cu375, and CuT-380A-QL; Mona Lisa N.V.) are made of a copper wire ($d_{\text{wire}} = 0.4 \text{ mm}$) helically wrapped around the stem of a T-shaped plastic core. The CuT-380A-QL has additional copper foil on the arms of the T-shape.

The Goldluna (Dr. Schittenhelm Pharma GmbH&Co.KG) is the only IUD containing a copper gold alloy wound around the stem of a T-shaped plastic core.

Two frameless models (Gynefix 200 with v.e., Gynefix 200 without v.e., both Gynlameda GmbH) consist of four cylindrically shaped copper elements strung on a nylon thread. One of these models has a visualization element (v.e.) to enable visualization during ultrasound imaging. It is made of surgical steel with dimensions of $2 \times 2 \times 0.4 \text{ mm}^3$. The third frameless model (IntraUterine Ball, mibe GmbH Arzneimittel) has 17 copper spheres wound onto a nitinol memory wire. All approaches yield a copper surface area of 200 mm^2 to 400 mm^2 .

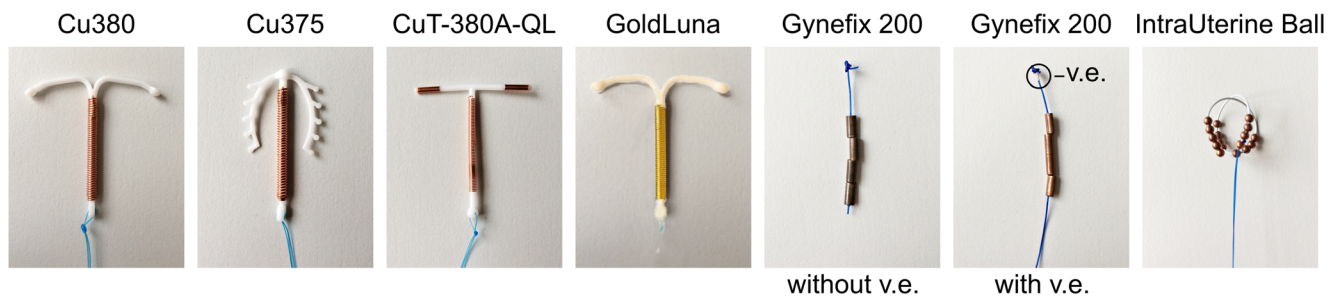


Fig. 1 Photographs of the investigated IUDs. The first three models (from left to right) contain a plastic core with a copper wire wound around the stem. The fourth model has a copper gold alloy wire wound around a plastic core. The next two IUDs are frameless with four hollow

copper tubes strung on a surgical thread. They differ in having a visualization element (v.e.) made of surgical steel at the top beneath the knot. The last model is designed spherically with 17 copper beads strung onto a nitinol memory wire

Scanner systems

MR experiments were performed in clinical 1.5 T and 3 T scanners (Magnetom Avanto, Magnetom Skyra) with an integrated 32-channel spine coil. CT images were acquired with a third-generation dual source multi-slice CT scanner (Somatom Force, Siemens Healthineers (all scanners)).

Tissue mimicking phantom

We designed a tissue mimicking phantom based on our experience in phantom design [27]. A cylindrical polypropylene container ($d = 120$ mm, $h = 150$ mm) was filled with 0.5% NaCl solution. Additionally, 0.375% NiSO_4 was added (Carl Roth (all chemicals)). NaCl increased the electrical conductivity of the liquid in order to simulate an electrical conductivity close to human soft tissue [28]. NiSO_4 reduced the relaxivity of water in MR [29] and provided tissue-mimicking susceptibility values.

IUD positioning

As clinical patient positioning is mostly conducted in a head-first supine orientation, we assumed an implanted IUD in the uterus to be aligned perpendicularly to the bore's main axis. This corresponds to an orientation perpendicular to the main magnetic field B_0 in MR scanners (Fig. 2). Similar positioning applies for CT imaging. The IUDs were oriented accordingly in the center of the phantom. Two locations in the scanner were evaluated. Position 1 was in the isocenter. Position 2 was at a distance of 25 cm outside and 25 cm to the left of the isocenter as imaging outside the uterus implies that the IUD is no longer located in the isocenter. Furthermore, a previous study has shown that the E-field distribution was in general strongest near the walls and that the local E-field is a critical factor in RF-related tissue heating [30].

MRI—temperature

Temperature assessment was performed with temperature fiber-optic probes (Optocon Fotemp, Weidmann

Technologies Deutschland GmbH) attached to the IUD (Fig. 2). The probes were placed at the upper and lower tip, as well as in the center of the copper element of the IUD [24]. Another probe was placed in the phantom at least 50 mm away from the IUD and recorded the reference temperature in the phantom. The temperature was logged every second with an accuracy of ± 0.2 K [31]. The phantom was stored in the scanner room 24 h prior to measurement to adjust to the scanner room temperature, approximately 22 °C.

A true fast imaging with steady-state free precession (TRUFI) sequence was employed. Imaging parameters at 3 T were echo and repetition time $TE/TR = 2.82/6.64$ ms, $FoV = 150$ mm \times 150 mm, flip angle $FA = 80^\circ$, and averages = 31. The predicted specific absorption rate (SAR) was on average 98% of the limit value in the normal operating mode. Total image acquisition time was 15 min. The parameters at 1.5 T were adapted to match the 3 T protocol. The scanner's ventilation was turned off. The measurements were first conducted at position 1 and repeated at position 2 (Fig. 2).

MRI—motion and torque

Motion assessment was performed with the IUD attached to a thread allowing free motion in the liquid. Gradient echo based (GRE) and TRUFI sequences were executed in all three major imaging planes (sagittal, coronal, and transversal). During measurement, the angular deflection was visually evaluated by an employee in the scanner room using an angular scale placed behind the IUD within the phantom.

Two additional scenarios were evaluated as clinical staff might also be affected when working at the bore entrance of the scanner in an upright position. In one setup, the IUD was placed in parallel to the main magnetic field in the middle of the bore entrance. In the second setup, the IUD was turned by 45° relative to its previous position to investigate a possible influence of the alignment to the magnetic field as suggested by [25, 32]. The motion and torque of the IUD were visually evaluated during the same sequences described above.

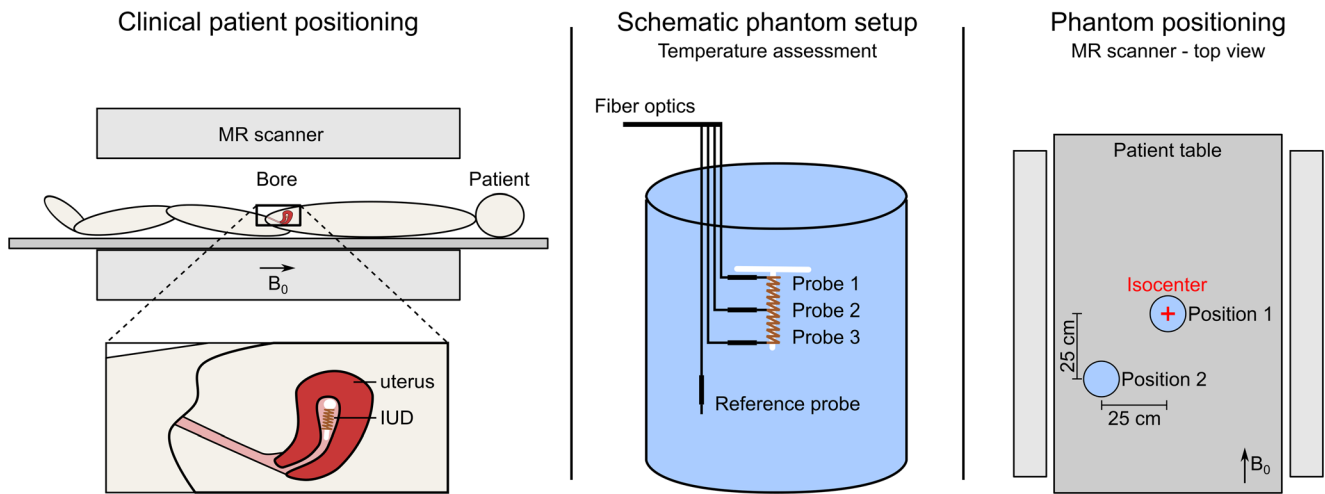


Fig. 2 *Left:* Schematic drawing of common clinical patient positioning (head first supine) in an MR scanner. The IUD is implanted in the uterus, which is located anterior posterior in the body for most women. Thus, the IUD aligns perpendicularly to the main magnetic field B_0 . *Middle:* Schematic phantom setup during temperature assessment. Three fiber-

optic temperature probes were positioned at the IUD, and one additional reference probe was placed in the phantom. *Right:* Positioning of the phantom at position 1 in the isocenter and position 2 at a distance of 25 cm outside and 25 cm to the left of the isocenter

MRI—artifacts

MR image artifacts were evaluated at 1.5 T and 3 T. Images were acquired with GRE, TRUFI, and turbo spin echo (TSE) sequences in all three standard imaging orientations. For each imaging orientation, two phase encoding directions were employed. Further imaging parameters are listed in Table 1. After imaging each IUD, phantom reference scans without the IUD were performed.

The artifact size was calculated in Matlab (The MathWorks, Inc.). A pixel in the MR image was defined as an artifact, if the signal intensity in the image with IUD changed by > 30% compared to its reference image [23]. The size of the artifact was then defined as a rectangle with its horizontal and vertical distance between the maximum edges of the artifact. An exemplary artifact boundary is shown in Fig. 3.

CT—artifacts

The phantom was scanned in CT with the following parameters: peak voltage = (80, 100, 120, 140) kVp, X-ray tube

current = (200, 400, 600) mA, and slice thickness = (0.5, 1.0, 2.0) mm, resulting in 36 parameter sets.

Further imaging parameters were kept constant: FoV = 512 pixel × 512 pixel, isometric pixel spacing = 0.74 mm, and spiral pitch factor = 1. The raw data were reconstructed using a smoothing kernel and an edge-enhancing kernel. A phantom reference scan without IUD placed was additionally performed.

For each parameter set, the mean HU μ_{ref} and its standard deviation σ_{ref} of the background liquid were determined in the reference image in a rectangular region of interest (ROI) measuring 160 pixel × 80 pixel.

A pixel in the image was classified as an artifact, if its HU_{image} was either

$$HU_{image} < \mu_{ref} - 3 \sigma_{ref}$$

or

$$HU_{image} > \mu_{ref} + 3 \sigma_{ref}$$

of the corresponding reference HU [33].

The percentage area of pixels classified as artifacts with regard to a 140 pixel × 140 pixel ROI centered at the object was calculated.

Table 1 Imaging parameters of MR artifact evaluation. Three sequences (GRE, TRUFI, and TSE) were employed. The parameters were kept similarly for at 1.5 T and 3 T, any deviations are due to scanner restrictions

| Parameters | 1.5 T | | | 3 T | | |
|----------------------------------|-----------|-----------|-----------|-----------|-----------|-----------|
| | GRE | TRUFI | TSE | GRE | TRUFI | TSE |
| TE (ms) | 10.00 | 1.41 | 12.00 | 10.00 | 2.47 | 13.00 |
| TR (ms) | 142.00 | 3.03 | 2200.00 | 142.00 | 4.94 | 2200.00 |
| FA | 25° | 70° | 171° | 25° | 70° | 171° |
| FoV (mm ²) | 140 × 140 | 150 × 150 | 140 × 140 | 140 × 140 | 150 × 150 | 140 × 140 |
| Resolution (pixel ²) | 64 × 64 | 64 × 64 | 128 × 128 | 96 × 96 | 128 × 128 | 128 × 128 |

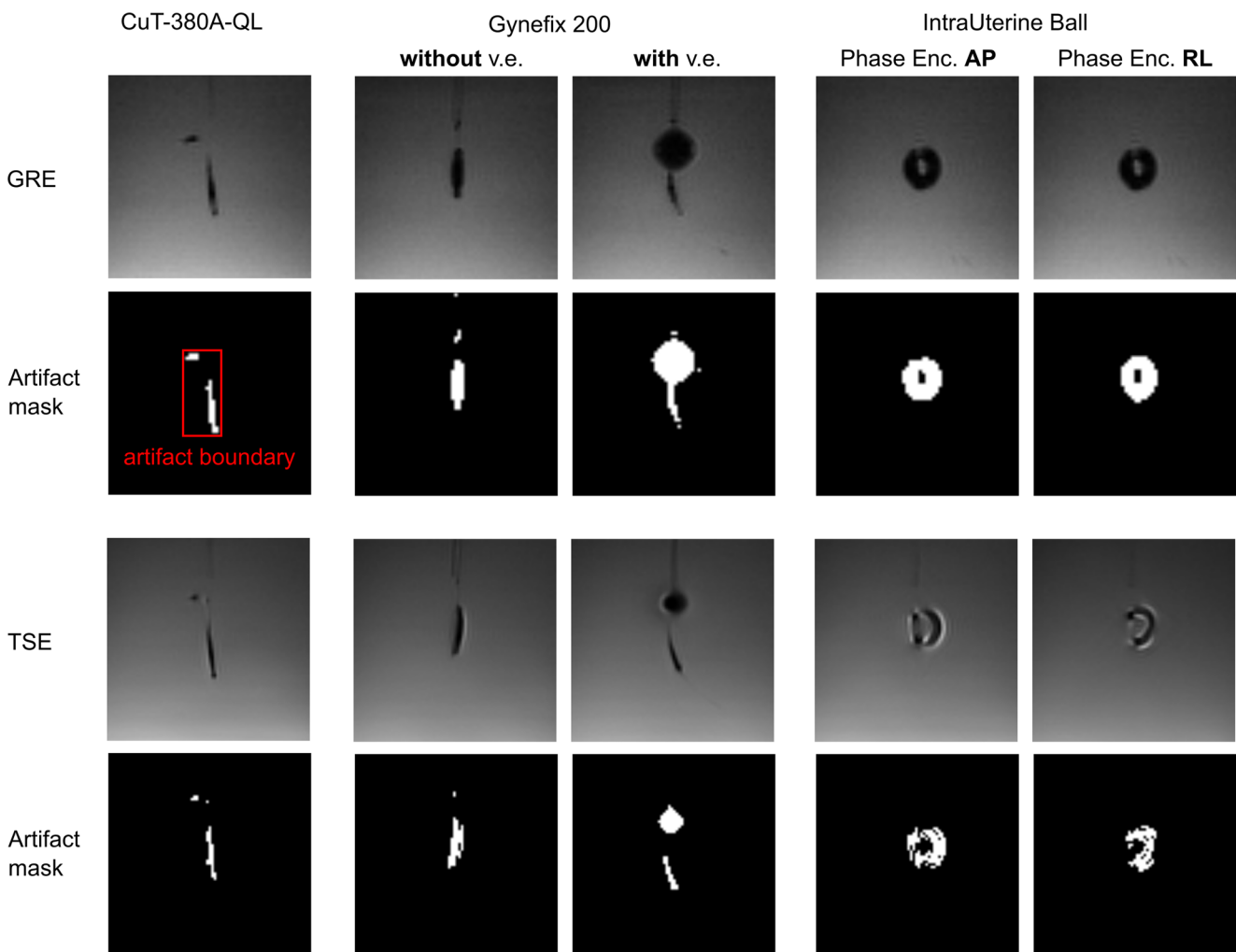


Fig. 3 Transverse MR magnitude images and corresponding artifact masks for selected IUDs. An exemplary artifact boundary (red) is displayed. *Top row:* GRE sequence. *Bottom row:* TSE sequence. *Left column:* The model CuT-380A-QL with copper foil on each arm of the T-shaped plastic core showing no significant artifacts except in its

vicinity. *Middle columns:* the model Gynefix 200 without v.e. (left) and with v.e. (right) showing the spherical signal loss around the v.e.. *Right column:* The IntraUterine Ball with anterior posterior (AP) and right left (RL) phase encoding directions. Subtle differences around the nitinol wire can be distinguished

Results

MRI—temperature, motion, and torque

No significant temperature increase was observed for any IUD under any tested conditions (Table 2). The maximum temperature increase at 1.5 T was measured as $\Delta T_{1.5T_{max}} = 0.6$ K for Gynefix 200 with v.e. at position 2 (Fig. 4). At 3 T, the maximum temperature increase was recorded as $\Delta T_{3T_{max}} = 0.6$ K for Gynefix 200 with v.e., Goldluna, and IntraUterine Ball at position 2.

Neither torque, i.e., angular deflection, nor translational motion was visually observed for any IUD at 1.5 T and 3 T in any imaging plane at any tested position.

MRI and CT—artifacts

The artifact during MRI was strongly limited to the vicinity of each IUD (Table 3). Cu380 and CuT-380A-QL had the largest artifact ($A_{\text{artifact}} = 2423 \text{ mm}^2$). However, the T-shaped IUDs already have a height of 36 mm and width of 32 mm resulting in $A_{\text{IUD}} = 1152 \text{ mm}^2$.

The v.e. of the Gynefix 200 caused a noteworthy spherical signal attenuation ($d_{\text{max}} = 18$ mm) surrounding the ($2 \times 2 \times 0.4 \text{ mm}^3$) v.e. (Fig. 3). Furthermore, the nitinol wire of the IntraUterine Ball caused noticeable signal attenuation (Fig. 3). The two phase encoding directions showed no obvious differences.

In CT, the artifacts mostly depended on the convolution kernel. For the smoothing kernel, the maximum percentages ranged between 38.0% and 75.5% for Gynefix 200 without

Table 2 Measured temperature increase of all IUDs at 1.5 T and 3 T at position 1 and position 2

| IUD | 1.5 T | | 3 T | |
|-----------------------|----------------|----------------|----------------|----------------|
| | Position 1 (K) | Position 2 (K) | Position 1 (K) | Position 2 (K) |
| Cu380 | 0.2 | 0.5 | 0.6 | 0.5 |
| Cu375 | 0.2 | 0.3 | 0.5 | 0.4 |
| CuT-380A-QL | 0.2 | 0.5 | 0.4 | 0.4 |
| GoldLuna | 0.1 | 0.5 | 0.5 | 0.6 |
| Gynefix 200 with v.e. | 0.2 | 0.6 | 0.5 | 0.6 |
| IntraUterine Ball | 0.3 | 0.5 | 0.5 | 0.6 |
| Reference probe | 0.2 | 0.3 | 0.3 | 0.3 |

Temperature increase at position 1 was significantly higher at 3 T compared with 1.5 T. The difference was not significant for position 2. Please note that only the Gynefix 200 with v.e. was tested, as the model without v.e. is structurally identical except for the v.e. made of surgical steel

v.e., and for the edge-enhancing kernel, the percentage ranged between 10.7% and 30.2% for Gynefix 200 with v.e. and CuT-380A-QL (Fig. 5).

Discussion

The presence of metallic implants puts patients undergoing an MR examination at risk and may impair image quality of CT scans. Heating or dislocation may occur. Moreover, the diagnostic quality of images may be impaired. This study characterized these interactions for copper-containing IUDs in a tissue-mimicking phantom. The MR temperature assessment showed no significant heating of any IUD, deeming them temperature-safe within the tested conditions. Also, no motion or torque of any of the tested IUDs was observed during MR measurements. Thus, all IUDs were regarded as motion-safe

Temperature curve: Gynefix with v.e. at 1.5 T in position 2

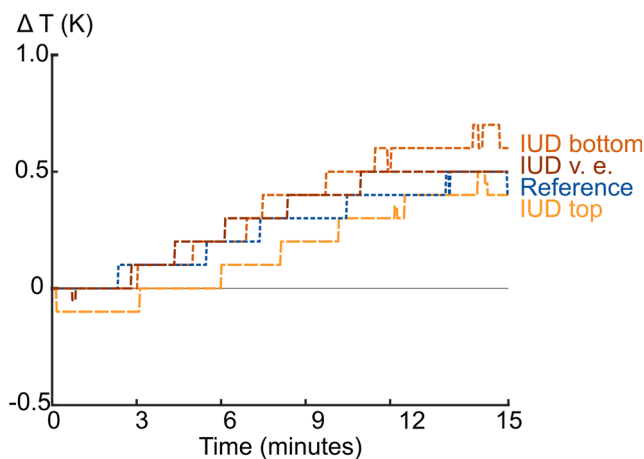


Fig. 4 Temperature curve for the Gynefix 200 with v.e. during 15 min of image acquisition employing a TRUFI sequence. One probe each was attached to the top and bottom of the copper tubes. A third probe was placed at the v.e. (displayed in shades of orange). The reference temperature probe is shown in blue. The increase in temperature is relative to the temperature measured prior to image acquisition

within the tested conditions. MR artifacts for all IUDs were restricted to the vicinity of the devices, except for Gynefix 200 with v.e. presenting signal attenuations surrounding the steel element. In CT, severe streaking artifacts were visible for all IUDs due to their metallic components.

Any temperature increase < 1 K complies with the limit value of norm EN60601-2-33 [26], deeming all tested IUDs as temperature-safe. Past studies demonstrated resonance effects on the tips of elongated cylinders. There, this effect yields elevated temperatures and is already observable for cylinders with a length equal to a half resonance wavelength of the RF pulse [34]. Yeung et al calculated the critical half resonance wavelength for RF wires during interventional MRI, resulting in $\lambda/2_{1.5T} = 173$ mm and $\lambda/2_{3T} = 111$ mm [35]. The height of the copper elements is smaller than 27 mm for all tested IUDs, and is thus significantly shorter than $\lambda/2$. This is in accordance with our results, as no significant increases in temperature were measured at the tips of the IUDs.

Santoro et al reported a temperature increase induced by a coronary stent of less than 3 K. The local/global specific absorption rate values applied in their study were more extreme than given by EN60601-2-33 [26]. Thus, their result suggests that the extra RF heating induced by a stent may be smaller, if not insignificant, if the norm is followed [12].

The temperature measurements were conducted with a 15-min TRUFI sequence depositing a high amount of RF energy in the tissue. We expect temperature rises at the IUDs to be even lower in vivo as (1) clinical sequences last rarely as long as our measurement interval, (2) the actual local RF power deposition will be significantly lower during clinical setups, and (3) blood circulation, i.e., perfusion, will dissipate heat.

Any angular deflection smaller than 45° is below the limit value stated in [25]. As neither torsion nor translation was detected during experiments, all tested IUDs were deemed motion-safe under the tested conditions. Regarding translational motion, a force that overcomes the frictional force F_R

Table 3 *Left:* Maximum artifact size of all IUDs at 1.5 T and 3 T evaluated according to the ASTM standard F2119-07 [23]. *Right:* Maximum percentage artifact of all IUDs for the smoothing and edge-enhancing kernel during CT imaging

| IUD | MRI | | CT | |
|--------------------------|--------------------------|------------------------|----------------------|---------------------------|
| | 1.5 T (mm ²) | 3 T (mm ²) | Smoothing kernel (%) | Edge-enhancing kernel (%) |
| Cu380 | 2110 | 2423 | 72.7 | 28.3 |
| Cu375 | 2211 | 1441 | 73.1 | 29.6 |
| CuT-380A-QL | 2423 | 2423 | 72.7 | 30.2 |
| GoldLuna | 1818 | 451 | 75.5 | 27.1 |
| Gynefix 200 without v.e. | 2211 | 2423 | 66.3 | 22.3 |
| Gynefix 200 with v.e. | 1909 | 922 | 66.7 | 25.7 |
| IntraUterine Ball | 2010 | 357 | 66.6 | 23.9 |

was calculated to be larger than 6×10^{-4} N (applying $F_R = \mu F_G$ with a coefficient of friction $\mu = 0.2$, and $F_G = m_{\text{IUD}}g = 2.6 \times 10^{-3}$ N). As no IUD visibly moved, the effective force acting upon the IUDs was even smaller than the calculated frictional force.

All IUDs, especially the IUDs containing solely copper, induced only small artifacts when introduced to the FoV in MR imaging. The maximum artifact size was lower at 3 T for the IUDs CU375, GoldLuna, Gynefix 200 with v.e., and IntraUterine Ball compared to 1.5 T. We assume this to be due to a shortcoming of the suggested method of the ASTM

F2119 standard. It defines the size of an artifact as a rectangle with the maximum horizontal and vertical distance in millimeters between the edges of the artifact. Furthermore, the standard suggests taking the slice with the maximum artifact size as a final result, and not an average value of multiple slices. Using this approach, a single outlier pixel can exorbitantly increase the size of the rectangle without a significant influence on image quality. In general, more prominent artifacts were observed for the other metals, namely surgical steel and nitinol. Here, alternative materials should be considered to minimize the impact on image quality and diagnostic errors.

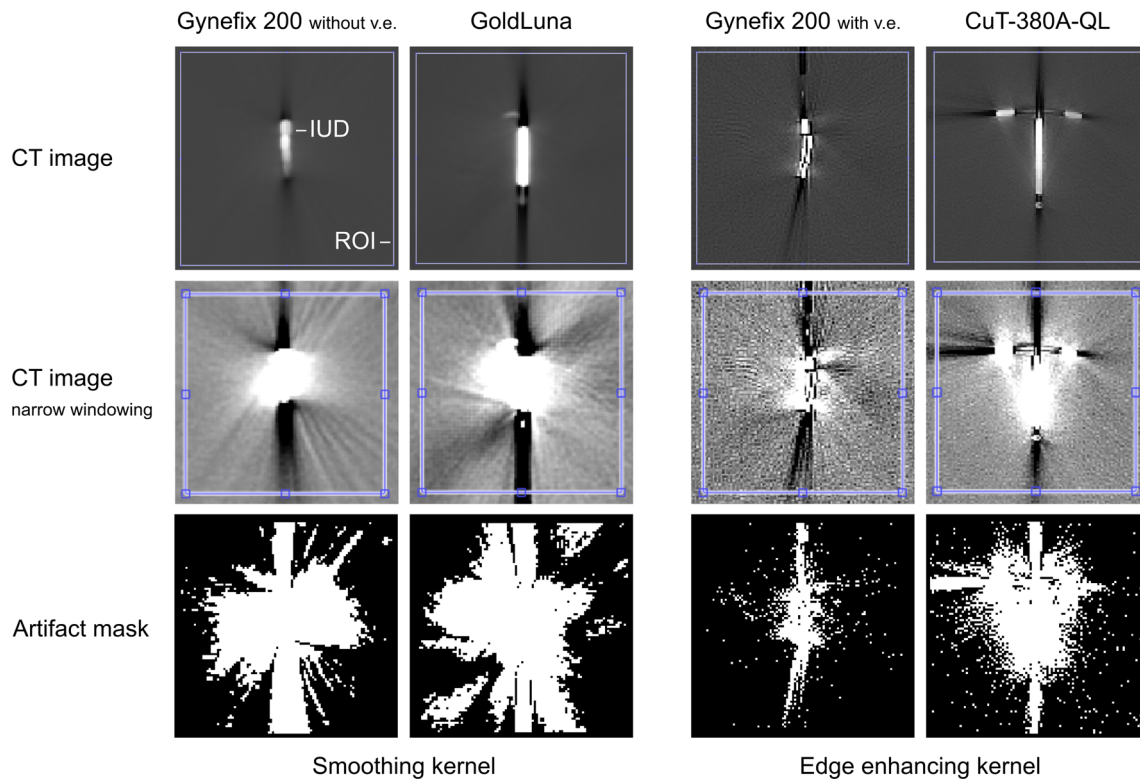


Fig 5 *Top and middle row:* CT images. *Bottom row:* Corresponding artifact masks for the maximum artifacts. *Left:* Percentage artifacts ranged between 38.0% and 75.5% for the Gynefix 200 without v.e. (at 140 kVp, 200 mA, 2-mm slice thickness) and GoldLuna (at 100 kVp, 600 mA, 0.5-mm slice thickness), respectively, for the smoothing kernel.

Right: Percentage artifacts ranged between 10.7% and 30.2% for the Gynefix 200 with v.e. (at 140 kVp, 200 mA, 0.5-mm slice thickness) and CuT-380A-QL QL (at 100 kVp, 600 mA, 1-mm slice thickness), respectively, for the edge-enhancing kernel. Narrow windowing: WL = 0, WW = 200 (left); WL = 0, WW = 400 (right)

All IUDs highly attenuated the X-ray beam during CT imaging leading to severe streaking artifacts [17]. Image and diagnostic quality may be degraded; however, this effect is clearly confined to the slices containing an IUD, i.e., the pelvic region. Higher voltage or X-ray tube current increase the likelihood of X-rays penetrating the metallic IUDs [16]. Therefore, artifacts are expected to be reduced with higher voltage or X-ray tube current [17], however at the expense of a higher radiation dose for the patient.

The observed effects, especially for MR imaging, might differ depending on the (1) IUD's orientation and location in the scanner, (2) models and design modifications, (3) measurement setup, and (4) applied coils, gradient setting, and field strength.

Firstly, we assumed IUD placement in the uterus perpendicularly to the main magnetic field. The implications for other orientations of the IUD with respect to the scanner, e.g., at a uterus prolapse, still need to be investigated.

Secondly, despite an extensive selection copper-containing IUDs commonly implanted in women, not every available model on the market was tested. Also, there are hormone-based IUDs using silver foil as ultrasound markers on the arms of the T-shaped core. The examination of those hormone-based IUDs was out of the scope of this study and could further be evaluated.

Thirdly, the experiments were performed in a homogeneous phantom, which is an important step prior to in vivo studies. Previous work has simulated the internal electrical field in body models for different gradient exposures [36]. The results demonstrated that the E-fields in the body may vary depending on the location and anatomical structures. In the pelvic region, elevated E-fields have been found. However, these are located at the hip bones and not in the center region, where the uterus is located. Thus, we assume that our homogeneous phantom is a valid approximation of the pelvic center region. However, to definitively determine the E-field variation of magnitude in the whole pelvic region under the influence of an implanted IUD, a future simulation study would be recommended. Also, future measurement setups for in vivo studies need to be altered, e.g., with MR thermometry instead of fiber-optic temperature sensor. As a remark, the torsion, however, does not depend on the heterogeneity of the body, since gradient fields are not influenced by it.

Fourthly, scanner modalities and their parameters vary widely. Our study focused on clinically realistic standard settings. Yet, higher field strengths and stronger gradients are available, and their influence must be examined.

We systematically evaluated the impact for women with implanted copper-containing intrauterine devices at clinical MR and CT scanners. Various models posed no significant risk possibly harming the patient, deeming MR examinations safe for women with an implanted copper IUD under the tested conditions. Image quality was more impaired for CT than for MR imaging and needs careful consideration during

diagnosis. Our results will help to increase patient safety and reassure staff in their daily clinical routine.

Acknowledgements The authors are grateful to Marius Siegfarth (Fraunhofer PAMP) for his assistance during temperature measurements.

The IUDs used for this study were supplied by the manufacturers who had no further influence on the study.

Funding information This research project is part of the Research Campus M²OLIE and funded by the German Federal Ministry of Education and Research (BMBF) within the Framework “Forschungscampus: public-private partnership for Innovations” under the funding code 13GW0092D.

Compliance with ethical standards

Guarantor The scientific guarantor of this publication is Frank G. Zöllner.

Conflict of interest The authors declare that they have no conflict of interest.

Statistics and biometry No complex statistical methods were necessary for this paper.

Informed consent Written informed consent was not required for this study because it was a phantom study.

Ethical approval Institutional Review Board approval was not required because it was a phantom study.

Methodology

- Prospective
- Experimental
- Performed at one institution

References

1. Kavanaugh ML, Jerman J (2018) Contraceptive method use in the United States: trends and characteristics between 2008, 2012 and 2014. *Contraception* 97:14–21
2. United Nations Population Fund (2016) TCu380A intrauterine contraceptive device (IUD) WHO/UNFPA technical specification and prequalification guidance. United Nations Population Fund, NY, USA
3. World Health Organization (ed) (2009) Medical eligibility criteria for contraceptive use – 4th ed. World Health Organization, Geneva
4. United Nations Department of Economic and Social Affairs (2011) World contraceptive use 2011. United Nations Department of Economic and Social Affairs, NY, USA. Available via http://www.un.org/esa/population/publications/contraceptive2011/wallchart_front.pdf. Accessed 01 Aug 2018
5. Dietrich O, Reiser MF, Schoenberg SO (2008) Artifacts in 3-T MRI: physical background and reduction strategies. *Eur J Radiol* 65:29–35
6. Guerin B, Serano P, Iacono MI et al (2018) Realistic modeling of deep brain stimulation implants for electromagnetic MRI safety studies. *Phys Med Biol* 63:095015
7. Golestani L, Angelone LM, Iacono MI, Katnani H, Wald LL, Bonmassar G (2017) Local SAR near deep brain stimulation (DBS)

- electrodes at 64 and 127 MHz: a simulation study of the effect of extracranial loops. *Magn Reson Med* 78:1558–1565
8. Nouredine Y, Kraff O, Ladd ME et al (2018) In vitro and in silico assessment of RF-induced heating around intracranial aneurysm clips at 7 Tesla. *Magn Reson Med* 79:568–581
 9. Bhusal B, Bhattacharyya P, Baig T, Jones S, Martens M (2018) Measurements and simulation of RF heating of implanted stereo-electroencephalography electrodes during MR scans. *Magn Reson Med*. <https://doi.org/10.1002/mrm.27144>
 10. Winter L, Oberacker E, Özerdem C et al (2015) On the RF heating of coronary stents at 7.0 Tesla MRI. *Magn Reson Med* 74:999–1010
 11. Tse ZT, Elhawary H, Montesinos CA, Rea M, Young I, Lampérth M (2011) Testing MR image artifacts generated by engineering materials. *Concepts Magn Reson* 39B:109–117
 12. Santoro D, Winter L, Müller A et al (2012) Detailing radio frequency heating induced by coronary stents: a 7.0 Tesla magnetic resonance study. *PLoS One* 7:e49963
 13. Elhawary H, Zivanovic A, Davies B, Lampérth M (2006) A review of magnetic resonance imaging compatible manipulators in surgery. *Proc Inst Mech Eng H* 220:413–424
 14. Christoforou EG, Tsekos NV, Özcan A (2006) Design and testing of a robotic system for MR image-guided interventions. *J Intell Robot Syst* 47:175–196
 15. Tse ZT, Janssen H, Hamed A, Ristic M, Young I, Lampérth M (2009) Magnetic resonance elastography hardware design: a survey. *Proc Inst Mech Eng H* 223:497–514
 16. Barrett JF, Keat N (2004) Artifacts in CT: recognition and avoidance. *Radiographics* 24:1679–1691
 17. Lee MJ, Kim S, Lee SA et al (2007) Overcoming artifacts from metallic orthopedic implants at high-field-strength MR imaging and multi-detector CT. *Radiographics* 27:791–803
 18. Kalender WA (2011) *Computer Tomography*, 3rd edn. Publicis MCD Verlag, Germany
 19. Mark AS, Hricak H (1987) Intrauterine contraceptive devices: MR imaging. *Radiology* 162:311–314
 20. Hess T, Stepanow B, Knopp MV (1996) Safety of intrauterine contraceptive devices during MR imaging. *Eur Radiol* 6:66–68
 21. Pasquale SA, Russer TJ, Foldesy R, Mezrich RS (1997) Lack of interaction between magnetic resonance imaging and the copper-T380A IUD. *Contraception* 55:169–173
 22. Berger-Kulemann V, Einspieler H, Hachemian N et al (2013) Magnetic field interactions of copper-containing intrauterine devices in 3.0-Tesla magnetic resonance imaging: in vivo study. *Korean J Radiol* 14:416–422
 23. ASTM Standard F2119-07 (2007) Standard test method for evaluation of MR image artifacts from passive implants. ASTM International, West Conshohocken
 24. ASTM Standard F2182-11a (2011) Standard test method measurements of radio frequency induced heating on or near passive implants during magnetic resonance imaging. ASTM International, West Conshohocken
 25. ASTM Standard F2213-06 (2006) Standard test method for measurement of magnetically induced torque on medical devices in the magnetic resonance environment. ASTM International, West Conshohocken
 26. EN60601 (2017) Medical electrical equipment - Part 2–33: particular requirements for the basic safety and essential performance of magnetic resonance equipment for medical diagnosis. Beuth Verlag, Berlin
 27. Neumann W, Lietzmann F, Schad LR, Zöllner FG (2017) Design of a multimodal ($^1\text{H}/^{23}\text{NaMR/CT}$) anthropomorphic thorax phantom. *Z Med Phys* 27:124–131
 28. Kato H, Kuroda M, Yoshimura K et al (2005) Composition of MRI phantom equivalent to human tissues. *Med Phys* 32:3199–3208
 29. Schuenke P, Koehler C, Korzowski A et al (2017) Adiabatically prepared spin-lock approach for T1 ρ -based dynamic glucose enhanced MRI at ultrahigh fields. *Magn Reson Med* 78:215–225
 30. Nordbeck P, Fidler F, Weiss I et al (2008) Spatial distribution of RF-induced E-fields and implant heating in MRI. *Magn Reson Med* 60: 312–319
 31. Optocon AG (2012). Reference manual for fiber optic thermometer FOTEMP1-4. Available via <http://www.optocon.de/en/products/fiber-optic-temperature-signal-conditioners/fotemp1-4-fiber-optic-single-channel-thermometer/>. Accessed 01 Aug 2018
 32. Shellock FG (2002) Biomedical implants and devices: assessment of magnetic field interactions with a 3.0-Tesla MR system. *J Magn Reson Imaging* 16(6):721–732
 33. van der Schaaf I, van Leeuwen M, Vlassenbroek A, Velthuis B (2006) Minimizing clip artifacts in multi CT angiography of clipped patients. *AJNR Am J Neuroradiol* 27:60–66
 34. Ulaby FT, Michielssen E, Ravaioli U (2015) *Fundamentals of applied electromagnetics*, global edition. Pearson Education Limited, Essex
 35. Yeung CJ, Susil RC, Atalar E (2002) RF safety of wires in interventional MRI: using a safety index. *Magn Reson Med* 47:187–193
 36. Samoudi AM, Vermeeren G, Tanghe E, Van Hoken R, Martens L, Josephs W (2016) Numerically simulated exposure of children and adults to pulsed gradient fields in MRI. *J Magn Reson Imaging* 44: 1360–1367